ORIGINAL ARTICLE

Development and Full Validation of a Monte Carlo Single-photon Emission Computed Tomography Camera Proposed for Coded Aperture Breast Tumor Imaging

Khalid Hussain[1], Mohammed A. Alnafea[2], Areej S. Aloufi[2], Alhanouf F. Alshedi[2], Hanan M. Assiri[3], Saqib Hayat[4]

[1]Department of Computer science and Information Technology, Faculty of Computer Science and Information Technology, The Superior University Lahore, Pakistan, [2]Department of Radiological Sciences, College of Applied Medical Sciences, King Saud University, P.O. Box 145111, Riyadh 4545, Saudi Arabia, [3]Department of Radiodiagnostic and Medical Imaging, Prince Sultan Military Medical City, Riyadh, Saudi Arabia, [4]European Laboratory for Non-linear Spectroscopy, University of Florence Italy, Campus Bio-Medico University of Rome, Italy

Abstract

Introduction: The Modified Uniformly Redundant Array (MURA) Coded Aperture (CA) imaging technique, initially developed for astronomical X-rays in far-field geometry, offers high Signal-to-Noise Ratio (SNR) and artifact-free imaging. Interest has grown in adapting MURA-CA to near-field geometry due to its high sensitivity and superior resolution, despite challenges related to artifacts. **Materials & Methods:** This study utilized MURA masks, anti-masks, and subtraction techniques to exploit their delta correlation function. Simulations were conducted with varying planar source sizes using 140 keV photons and Gaussian blurring to replicate real-world conditions. Separate decoding functions were applied to reconstruct images from mask- and anti-mask-projected data. Metrics including resolution Full Width at Half Maximum (FWHM), contrast, SNR, root-mean-square error (RMSE), and correlation coefficients were evaluated. **Results:** MURA-CA exhibited significant SNR advantages compared to pinholes and collimators. Near-field imaging, however, introduced artifacts that could be mitigated by transitioning to far-field geometry, though at the expense of counting efficiency and SNR. Subtraction of mask and anti-mask images effectively minimized side lobe effects and reduced RMSE, achieving results comparable to individual mask and anti-mask projections. Further enhancements were made by optimizing the trade-off between SNR and resolution under fixed time and dose conditions. **Conclusion:** MURA-CA is particularly well-suited for far-field applications like breast tumor imaging, where artifacts are minimal. This study highlights the potential of a MURA-CA system specifically designed for high-resolution SPECT imaging, integrated with a clinical gamma camera, to enable early tumor detection with improved imaging performance.

Key words: Coded aperture imaging, Monte Carlo, modified uniformly redundant array, single-photon emission computed tomography camera, validation

INTRODUCTION

The precise localization of lesions using Monte Carlo Simulation (MCS) is a dynamic area of research. MCS is a computational technique for modeling and solving complicated issues that involves creating a random sample of input variables and evaluating their effects on the output file.[1] The technique is used in various fields, including engineering and physics, such as traffic flow or energy distribution.[2] Imaging modality, such as single-photon emission computed tomography (SPECT), relies on MCS to develop, test, and validate models before implementation on physical machines.[3] The process of MCS involves several steps.[4] The first step is to define a numerical model that represents the Modified Uniformly Redundant Array-Coded

Address for correspondence:
Khalid Hussain, Faculty of Computer Science and Information Technology, The Superior University Lahore, Pakistan.
E-mail: khalidhussain.fsd@superior.edu.pk

Received: 25-07-2025
Revised: 20-09-2025
Accepted: 27-09-2025

Aperture (MURA-CA) system along with a clinically sized gamma camera. It includes input variables (i.e., parameters) that affect the Coded Aperture (CA) imaging system's behavior and an output of interest. Next, random samples are generated from the probability distributions assigned to the input variables. The number of samples generated depends on the desired accuracy and precision of the simulation. The following step is to run the model, i.e., for each set of randomly generated input values, the model is executed to compute the corresponding output. The model may involve mathematical equations, simulations, or other computational methods. Finally, to understand the behavior of the system and create predictions, the output values generated by many simulations are finally gathered and examined. Techniques for statistical analysis are frequently used to compile, interpret, and gain an understanding of the range of potential outcomes. Thus, this study aimed to utilize the method to simulate particle bio distribution within the human body, serving as a powerful potential tool for investigating photon emission and transmission through biological tissues.

Moreover, a rotating gamma camera is used to perform SPECT scanning around the patient's body. The primary focus of the gamma camera's design is the radiation focusing component, which is performed through a collimator or a CA mask. To improve spatial resolution and sensitivity while lowering the patient dosage to the lowest possible level, CA imaging techniques were developed as an alternative to parallel hole collimators.[5]

Imaging gamma (γ) rays at energies more than a few keV is challenging since it is frequently impossible to concentrate on these photons using standard mirrors or lenses. To address this issue, a type of geometrical collimator, such as a pinhole camera, was developed. CA attempts to retain high signal throughput while achieving small pinhole resolution. The core idea is to address photon scarcity by incorporating numerous small pinholes instead of a single large one.[5] The image is created in a position-sensitive detector after the gamma flux travels through a hole in an opaque plate.

Because of its delta function response (≈ δ), the pinhole camera possesses perfect imaging qualities. Despite having a narrow field of view (FoV), it generates high-resolution images. However, due to its small hole size, this direct-imaging device has low efficiency and requires considerable imaging time. Therefore, it is noted that a low signal, poor-quality image is produced due to the fact that there are typically few γ-ray photons detected. The collimator imaging, such as the parallel hole, is limited by the design and also provides a low detection efficiency.

A camera with many pinholes was proposed as a solution to obtain a much larger fraction of the incident flux, and permits high-resolution imaging. The image produced from such a camera is based on the principle of" Spatial Signal Multiplexing." It simply means that every incident point source, within the object FoV, is participating in encoding the flux into a predetermined pattern or code, thus called CA or mask, which casts a shadow of this pattern onto the detector surface. The encoded pattern (projected image) is then decoded to produce a usable image, usually by comparing the pattern of the encoded image with the pattern generated by a point source. This type of imaging is hence a two-step procedure. To recover or rebuild the image from that source, the process starts with encoding (multiplexing) the source information and concludes with decoding (de-multiplexing). The primary motivation for this indirect image generation is the expectation that, in comparison to collimator-based imaging systems, it will combine a greater signal-to-noise-ratio (SNR) because of the CA's large open area with a higher resolution because of image magnification.[6-8] MURAs are regarded as the optimal choice for coded mask design patterns due to their minimal side lobes. These side lobes greatly influence the projected image, affecting quality parameters such as spatial resolution, contrast, and SNR. Consequently, the MURA-CA mask is considered the most suitable pattern among CA designs due to its reduced side lobes.[6,9] Thus, several Monte Carlo codes are now used for medical imaging, such as Monte Carlo N-Particle,[10] Penetration and Energy Loss of Positrons and Electrons,[11] Geometry and Tracking 4 (Geant4)[12] and its derivative Geant4 Application for Tomographic Emission (GATE).[4]

Therefore, this study aims to develop and fully validate a Monte Carlo SPECT simulation for coded aperture breast tumor imaging, utilizing a Modified Uniformly Redundant Array (MURA) mask to enhance image quality through high sensitivity and superior resolution in near-field geometry. The approach also enables further exploration of MURA configurations for radionuclide imaging in early breast tumor detection. To support this goal, the study includes the development and evaluation of a CA system specifically designed for high-resolution single-photon planar imaging using a SPECT setup integrated with a conventional gamma (Anger) camera.

MATERIALS AND METHODS

The basis of the simulation code is a module that determines the location where the shadow cast by a single mask hole from a point source falls on the detector's pixel grid. A simulated system consisting of a planar source and MURA mask/anti-mask[13] was generated by GATE [Figure 1]. The detector is built of sodium iodide (NaI), has an area of 19.1 × 19.1 cm^2, and is filled with 3.67g/cm^3 density NaI material that is 0.9525 cm thick. The detector was pixelated with a pixel size of 2 mm × 2 mm. The backscatter from the photo-multiplier tube (PMT) array is estimated by modeling a 6.8 cm thick slab of Pyrex, following the approach suggested by DeVries and Moore (1990).[12] The backscattering compartment measured 19.1 × 19.1 × 6.8 cm^3. The tungsten MURA mask/anti-mask had dimensions of 8.2 × 8.2 × 0.15 cm^3, with a fixed hole size of 0.02 cm^2, and provided approximately 99% attenuation for typical incoming gamma rays of 140 keV.[14] Given that the mask is 30 cm from the detector and the source is 10 cm, the magnification factor is 4, which may be calculated as follows: 4 (m = 1 + b/a),[8] where a represents the distance from the object to the mask, and b is the distance from the mask to the detector. Mask holes are assumed square, and the code finds the location of the hole on the imaging detector.

Verification of the simulation

To validate the simulation data, it is required to have an accurate and detailed experimental knowledge of the gamma camera response function. This is necessary to have confidence that the geometry and simulation results are accurate. To simulate the response function of the gamma camera detector, first the resolution function of the camera needed to be modeled. Both the energy deposition and the spatial resolution function of the gamma camera were expected to be closely approximated by a Gaussian response. This indicates that simulating a physical γ-camera, both Gaussian spatial blurring and Gaussian energy blurring are essential. Initially, due to the restricted spatial resolution seen in real-world imaging conditions, the recorded (X, Y) spatial information is blurred. The spatial blurring was done by sampling a Gaussian distribution with full width at half maximum (FWHM) = 0.37 cm, which corresponded to the camera's inherent resolution as specified by the manufacturer. This phenomenon occurs with real gamma cameras when the PMT records an incorrect image. In the simulated data, the actual (X, Y) spatial information is blurred by a Gaussian with σ = FWHM/2.35 = 0.1574. In a similar way, recording the energy deposition process is subject to Gaussian broadening, which is accomplished by sampling a Gaussian with an energy-dependent FWHM. The FWHM energy dependency was measured experimentally using spectra obtained from a previously mentioned Toshiba gamma camera. Many mono-energetic gamma sources (^{201}Tl, ^{57}Co, ^{99m}Tc, and ^{51}Cr) that range from 72-320 keV peak energies were experimentally imaged in air without scattering material. The FWHM values associated with these energy spectra were fitted to a function [120] that relates the energy deposited to the FWHM of the energy response $FWHM = n_1 \times E^{1-n2}$

where n_1, n_2 are values indicating the most appropriate fit to the experimental data and the simulated results from the CATE, and E is the energy deposited. The Matlab algorithm uses the previously described functional model to blur the energy deposited. Relying on the above energy spectra measurements, using the actual Toshiba gamma camera, and using $FWHM = n_1 \times E^{1-n}{}_2$, the best fit was found with $n_1 = 0.35$ and $n_2 = 0.23$ as demonstrated in Figure 2.

Particle interactions are recorded in the area designated as the sensitive detector inside the scanner's geometry. These interactions result in hits inside the sensitive detector. Each hit provides information such as the amount of energy deposited, the position of the interaction, the kind of interaction, and the origin of the particles. The energy window was defined using built-in modules in the GATE digitizer,[15,16] which also applied blurring to both energy and position. Gaussian blurring was used for both energy and location, with an energy window set at 10% of the 140 keV energy.

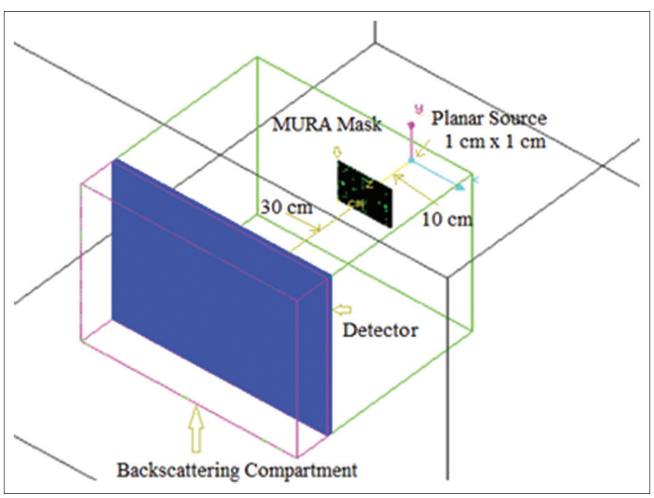

Figure 1: A schematic depiction of the Monte Carlo Simulation with a 99mTc photon energy (140 keV) square source employing Modified Uniformly Redundant Arrays- Coded Aperture in the near-field imaging geometry. A 0.95 cm NaI scintillation detector makes up the image detector. It is seen that 10 cm² separates the source from the mask, and 30 cm² separates the mask from the detector

Challenges in designing near-field MURA imaging

Choosing an optimal size and pattern to design a mask is a complex task.[17] In coded aperture imaging, the mathematics indicate that ideal point-spread functions are achieved with apertures possessing strong correlation properties in far-field

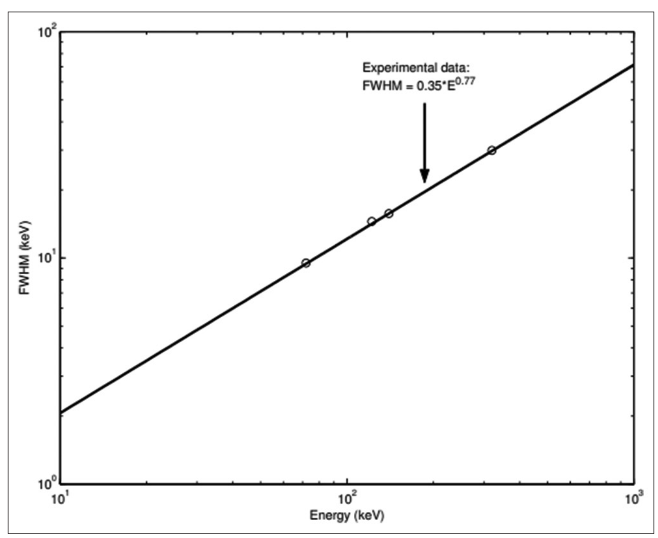

Figure 2: The association between the full energy peak (FWHM) and the energy deposited in the detector. Unfilled circles reflect experimental data

conditions. In near-field imaging, however, several factors can cause deviations from this optimal state, as rays from the same point source within the object are not parallel. The primary challenges in designing the coded mask stem from the object's finite thickness and the intensity modulation of the aperture's projection on the detector, influenced by variations in the gamma rays' incidence angle.

Another critical design factor is maximizing the mask's throughput while minimizing the patient's radiation dose. The MURA pattern is preferred for clinical applications, as it reduces patient dose by featuring a 50% open area that is transparent to radiation. In addition, variations in the angles of incoming photons lead to intensity modulation in the images projected onto the detector, creating artifacts in the reconstructed images.[18] To avoid these artifacts, in addition to geometric design, an upgraded decoding algorithm is required. Using our subtraction and decoding approach, we can create a delta-like correlation function on a MURA-based aperture while minimising background noise. Non-linear photon flow, an off-centre source, and the detector's restricted size may all contribute to background noise.[14]

Mura parameters and physical consideration

For optimum imaging with MURA masks of finite size, the whole encoded pattern must be projected onto a scintillation detector and decoded using correlation.[19] Mask design parameters are crucial for attaining perfect imaging qualities since suitable dimensions have a direct influence on the quality of the projected image. The mask's planar dimensions depend on its specific clinical application and the camera size, with Tungsten (W) and Lead (Pb) being the preferred materials due to their high attenuation capabilities. Tungsten, with a thickness of 1.5 mm, offers 99.4% attenuation, effectively reducing the detection of oblique particles outside the FoV.[20] Studies analysing masks constructed from tungsten and lead of varying thicknesses have shown that tungsten at 1.5 mm thickness provides the best point spread function (PSF) compared to lead and other thicknesses.[21] Hole shapes can be hexagonal, cylindrical, or box-shaped, but box-shaped holes yield better quality factors.

In this study design, a tungsten mask with a 1.5 mm thickness and dimensions of 8.2 cm × 8.2 cm was used. In addition, square holes measuring 2 × 2 mm, arranged in a 41 × 41 binary array pattern, were utilized to investigate the mask/anti-mask configuration.

The design of the coded mask

For optimal image performance, the autocorrelation function of the mask pattern should ideally resemble a delta function. Alnafea[9] investigated several mask designs, including the binary Fresnel zone plate (FZP), the sinusoidal zone plate, the L and X-shaped arrays, the non-redundant array, the uniformly redundant array, and the MURA. The FZP, non-redundant, X, and L shapes have been demonstrated to contain side lobes that cause image artifact when employed for reconstruction; hence, they are not regarded as the best design alternatives for usage in clinical settings. Yet, cyclic difference sets, including URAs and MURAs, have been explored as among the most promising coded aperture patterns with favourable transmission characteristics (a 50% close/open area, i.e., the regions that are transparent and those that are opaque to gamma rays are identical) and flat (zero) side lobes.

This study utilized the MURA mask and anti-mask originally developed by Fenimore and Cannon[22] and later refined for the presented simulations. The binary mask array consists of a pattern of 0s and 1s, where 0s denote opaque areas and 1s signify openings that permit gamma rays to pass through, recording flux on the detector. Each box-shaped opening measures 2 × 2 mm and is mounted within a fixed holder measuring 19.1 × 19.1 cm. The mathematical representation of mask Aij and its decoding mask Gij is given by[5]:

$$A_{ij} = \begin{cases} 0 & if\ i = 0; \\ 1 & if\ j = 0,\ i \neq 0; \\ +1, & if\ C_i C_j = +1; \\ 0, & otherwise \end{cases} \tag{1}$$

Were

$$C_i C_j = \begin{cases} +1, & if\ i\ is\ are\ sidue\ modulo\ L; \\ -1, & otherwise \end{cases} \tag{2}$$

Where L = 4m +1, and m=1,2,3,4,…. all prime numbers can be used for designing CA from Equation (1). The G function is the inverse of A and is generated from the aperture mask based on the following equation:

$$G_{ij} = \begin{cases} +1, & if\ i + j = 0; \\ +1,\ if\ A_{ij} = 1, & (i + j \neq 0;) \\ -1,\ if\ A_{ij} = 0, & (i + j \neq 0;) \end{cases} \tag{3}$$

Equation (3) is applied to aperture A, producing a decoding array G that is utilized to decode the projected picture. In this scenario, all 0s are transformed to −1 and all 1s to +1, except for the 0 term at ij=0, which is altered to +1. Figure 3 depicts three-dimensional plots of decoded mask and anti-mask images with ideal features and a delta PSF. The PSF is entirely flat and has no side lobes, suggesting that the MURA-CA pattern is optimal for radionuclide breast cancer applications.

CA image formation procedure

This section provides a brief description of the decoding procedure of MURA-CA image formation. First, it involves generating the decoding function "G function" as described in Equation 3. It depends on the type of aperture used in the encoding process. As O indicates the reconstructed object image, D becomes the projected image on the detection plane, and G represents the decoding function, then O can be obtained by applying the cross-correlation theorem to the decoding function G and D, the projected raw image,[5,23,24] which is obtained by running the GATE simulation.

$$O = D \otimes G \tag{4}$$

Figure 4 illustrates how the reconstructed object image is obtained, thus showing the projected image as a square in addition to the decoding function.[9]

The raw projected image on the detector is taken by the MURA-CA correlation method to correlate it with the decoding function. In separate simulations, both mask and anti-mask were applied for encoding to assess performance by measuring the full width-at-half maximum (FWHM), contrast, signal-to-noise ratio (SNR), root-mean-square error (RMSE), and correlation coefficients from the decoded images. Note that the decoding function should be adjusted to be rescaled according to the magnification factor. The latter depends on the distance between the object, aperture, and detector in near-field imaging applications. In addition,

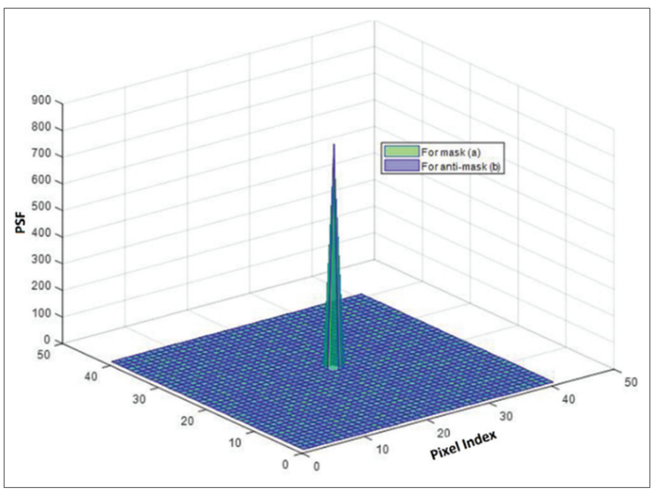

Figure 3: The delta function of the binary mask (a), and (b) the anti-mask. Both masks were demonstrated with scaling factor of 4

contrast, which serves as a measure of lesion visibility, can be specified by normalizing the lesion signal (S) to the background signal (B)[25] as:

$$C = \frac{(S - B)}{B} \tag{5}$$

The region of interest (ROI) determines the value of the signal, defined as a square area twice the size of the FWHM. The background signal, B, was measured by averaging over an area six times the FWHM, excluding the ROI. Image contrast was calculated for all obtained images of different source sizes. This is important to assess contrast alongside other image evaluation parameters. The error bars representing variations in image contrast from repeated simulations were also calculated to illustrate deviations around the mean value.

Image profiles of the mask, the anti-mask, and their difference

Image profiles of MURA masks were calculated as demonstrated in Figure 5. It illustrates the 2D profiles of images for the mask, the anti-mask, and their difference. It is worth pointing out that each projected image is decoded with its respective decoding function G. It is clear from the figure that the trend of all plots has little variation with each other. Thus, its shape is symmetrical on both sides of the peak value. The subtracted image, shown with a black asterisk line, exhibits a symmetrical shape on both sides of the central peak. Consequently, it has effectively reduced background noise through decoding with either the mask or anti-mask decoding function. To further investigate the data, we looked at all values lie, i.e., display the confidence interval, and see if around 68% of scores are within 1 standard deviation of the mean and error bar measured. It basically represents the mean±standard deviation ($u \pm \sigma$). Comparable values for image characteristic parameters are shown by the subtracted image.

RESULTS

All experiments were conducted first by using a set of simulations with the mask and then with the anti-mask. In

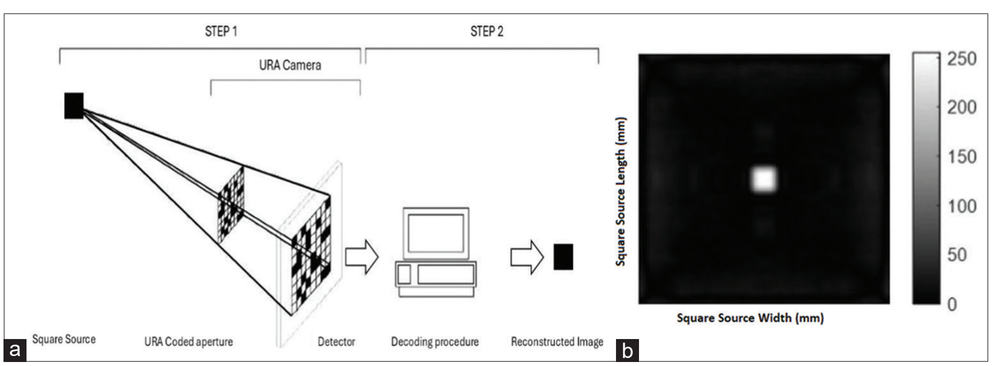

Figure 4: (a) Illustration of the coded aperture (CA) imaging principle for a square source demonstrating the two steps of CA image formation, (b) the decoded image

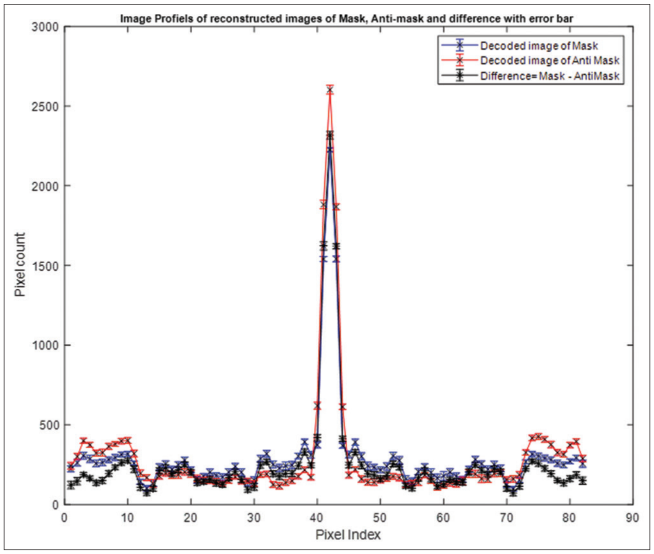

Figure 5: Quantification of the Monte Carlo Simulation data of Modified Uniformly Redundant Array-Coded Aperture camera illustrating the image profiles for the mask (blue circle line), the anti-mask (red dotted line) and their subtracted image (black line with asterisk). All the 2D plots for a planer source of 1 × 1 mm with activity of 15 mCi for 1 s

both designs, an aperture was located at a distance of 10 cm from the source and scintillation detector. The simulations were then repeated with planar square sources of varying sizes, from 1 mm² to 4 mm², for both setups. The radioactive source activity was set at 15 mCi and simulated for 1 s, remaining consistent across all simulations. An in-house MATLAB code was created for post-processing and data analysis. Thus, enabling the interpretation of raw projection data from GATE simulations to assess image performance parameters.

Analysis of obtained images

Since all masks have an opening of 50% substantial number of photons passes through the mask, allowing energy deposition on the detector and thus an optimal image. The images were decoded by correlating them with the G function, as illustrated in Equation 3 and Equation 4, respectively. The result of the projections of the mask, the anti-mask, the decoded images, and their difference are shown in Figure 6.

The projection difference is analyzed further by decoding with the mask g function and the anti-mask g function. It is worth pointing out that exactly the same characteristics in both cases of the decoding functions were observed. The 2D plots of the decoded images, which exhibit symmetrical shapes on both sides of the axis, are shown in Figure 7.

Interestingly, the projected images have the same value as the sidelobe in both cases. Figure 7 illustrates either decoding with the mask decoding function or by the anti-mask decoding function. Consequently, better resolution and less background noise are calculated from the mask and the anti-mask, and this proves the advantage of MURA-CA for small tumor breast detection.

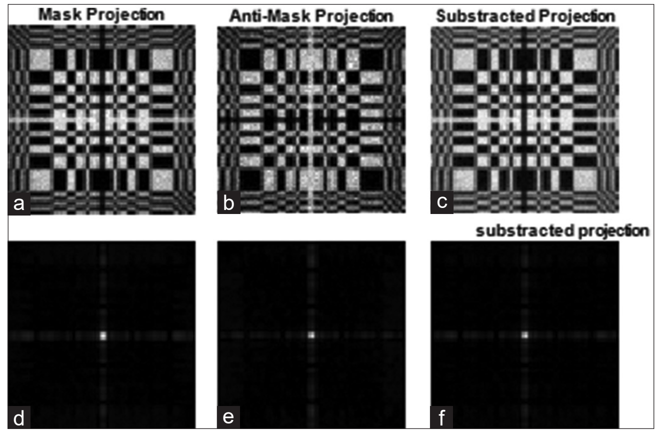

Figure 6: The projected images of (a) the mask, (b) the anti-mask, (c) their difference, (d) the decoded image of the mask, and (e) decoded image anti-mask and (f) decoded image of subtracted projections

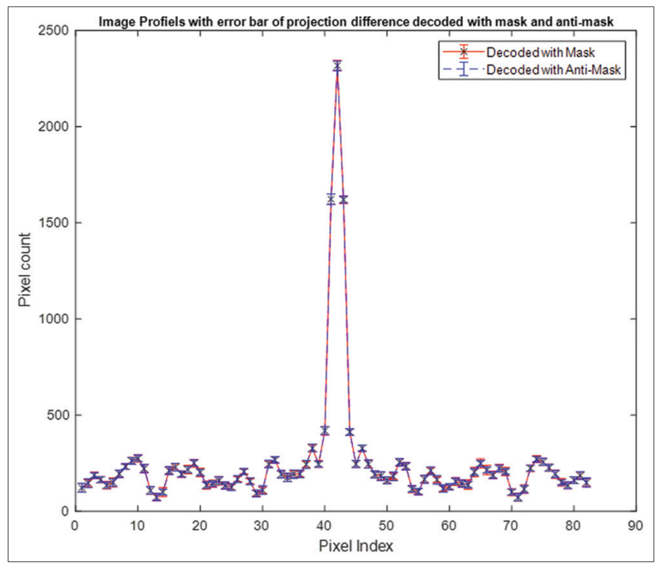

Figure 7: The decoded images and the corresponding profiles obtained from the Monte Carlo Simulation s of a square source of 1 mm² illustrating no projection difference of the mask and the anti-mask

Resolution

Since a CA camera's overall spatial resolution is mostly influenced by the detector's intrinsic spatial resolution (3.7 mm in this case), the chosen geometry gives an object magnification of 4. The mask is based on an 83 × 83 MURA pattern and is comprised of 2 × 2 mm² tungsten elements with a thickness of 1.5 mm. It provides ≈ 99.4% photon attenuation for 140 keV photons at normal incidence. The calculated system spatial resolution was done at full width half maximum (FWHM)[26] for variable-sized sources and is presented in Figure 8.

The FWHM for the obtained images of the mask, the anti-mask, and the decoded subtracted projection. The source sizes were varied from 1 mm² to 4 mm². The resolution in the case of decoded subtracted projection has a comparable value with both the mask and the anti-mask.

Contrast

The energy window peaking for the gamma camera has a proven effect on the planar images. This study proved the effect on the contrast of the MURA-CA obtained images. Thus, the image contrast of different source sizes was estimated to check the CA image contrast. The error bars for the contrast from numerous simulations of various experiments were also computed. Such results showed variation around the mean value. Detailed contrast plots are shown in Figure 9a, illustrating a linear decrease as the size of the square source increases.

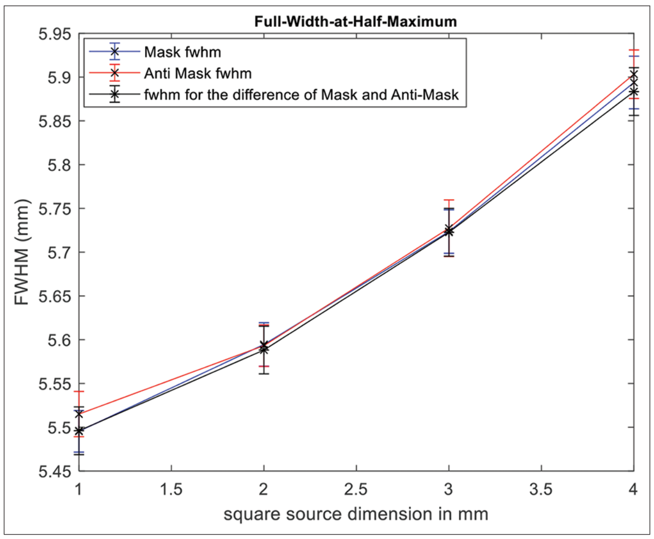

Figure 8: Quantification with Modified Uniformly Redundant Array-Coded Aperture camera in detecting the full width at half maximum as a function of source sizes. All sources were planar square sources ranging in size from 1 mm² to 4 mm²

Figure 9a illustrates that by increasing source dimensions for the mask, the anti-mask, and their difference, the image contrast decreasing. In other words, the smallest source has a better value of contrast and thus better localization of the lesion area. Since the subtraction of both has reduced the effect of sidelobes, it reported a better value of contrast as compared to mask and anti-mask.

Quantification of RMSE

The RMSE is a measurement of the average difference between a model's predicted and actual values. RMSE calculated for projected images of the mask and the anti-mask with reference to the ideal image. The subtracted image has a lower RMSE[27] compared to the mask and anti-mask images. The reference image was generated by correlating the binary matrix of the mask with its decoding (G) function as shown in Figure 3. The linear relationship among the RMSE of the mask, the anti-mask, and the subtracted image is illustrated in Figure 9b. It basically presents the RMS values for the mask, anti-mask, and the image obtained from the subtraction of both projected images. The ideal image served as a reference for calculating the RMSE of square sources of different sizes. The RMSE value for the subtracted image is lower than that of the mask and the anti-mask for all simulated sources. Thus, the reduced RMSE value for subtracted images, along with diminished background noise, yields more favorable values for image characteristic parameters compared to the mask and the anti-mask alone.

Correlation coefficients

The MURA-CA correlation coefficient measures the strength of a linear link between two images. The values of it might vary from −1 to 1. A perfect negative, or inverse, correlation is represented by a correlation coefficient of −1, with values in one series rising while values in the other drop, and vice versa.[28] Its maximum value is 1, representing a perfect

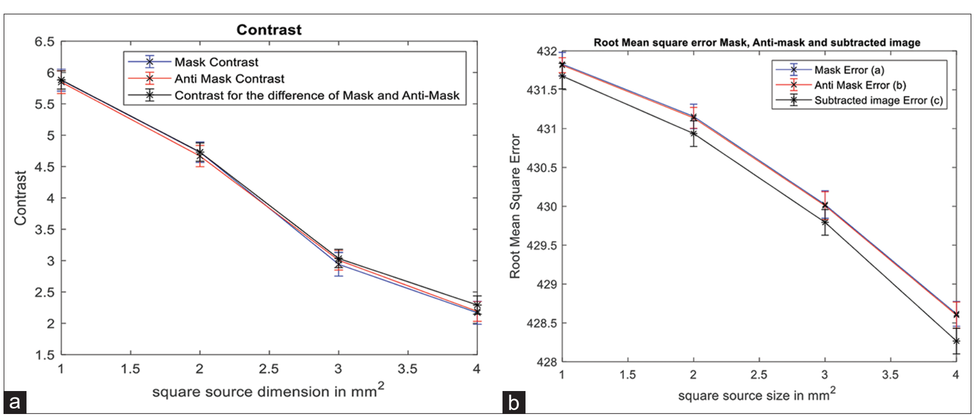

Figure 9: Quantification of the Monte Carlo Simulation data of Modified Uniformly Redundant Array-Coded Aperture camera in detecting (a) signal from square source; values calculated from data images of mask, anti-mask, and subtracted images as a function of increasing source sizes. And (b) the mean square error for mask, anti-mask, and subtracted mask/anti-mask image relative to the reference image

match, such as when comparing an image with itself. For two distinct images, the closer the coefficient is to 1, the stronger their relationship. The correlation coefficients for the mask, the anti-mask, and the subtracted images across different sources were calculated. Then compared them with the reference image. Figure 10 displays the correlation between the subtracted images, the mask, the anti-mask images, and the reference image. All the image data were for square sources of different sizes. The data presented included the error bars. The subtracted image has a correlation coefficient near 1, indicating a stronger correlation with the reference image than the mask and the anti-mask images. Thus, the subtraction method demonstrates superiority over the individual mask and the anti-mask.

DISCUSSION

This work presents and analyzes the realistic simulation and validation procedure for a clinical gamma camera. Monte Carlo Simulation (MCS) is being carried out in this study utilizing a well-known GATE program, which will be used subsequently to continue investigating the potential uses of MURA-CA radionuclide imaging for breast tumor imaging. The steps for modelling and validating the simulated camera against the full-size clinical Infina gamma camera are outlined. Such imaging verification processes are critical for providing confidence in simulation work. It outlines the methodology used to model and evaluate the Infina gamma camera's image formation with parallel-hole collimators. The obtained findings utilizing MSC and real-world experiments with the gamma camera reveal accurate construction, testing, and verification of simulated geometry. Furthermore, the 2D set of experiments reveals that the main cause of distortion artifacts in near-field geometry is the source object's finite distributed size, primarily from within the focal plane. It also implies that the shape and amplitude of the artefact's side-lobes can be predicted based on such imaging geometry. The above results compared the predicted flat field distortion of a 2D uniform square source object. Figure 10 presents the predicted flat field distortion of size 1×1 cm^2 up to 4×4 cm^2 produced from MCS data. The result of this study explains that the MURA aperture with the mask and the anti-mask have slight differences in values. It is also suggested that MURA is highly effective for imaging small tumors. A key finding of this study is the prediction of the artifact from an extended source. A significant difference in the side-lobes of subtracted images from the mask and the anti-mask. The results of the simulations demonstrate that with near-field artifacts corrections, the MURA-CA approach shows good performance for small lesion detection in breast cancer applications. This is because the subtraction method has reduced background noise in the reconstructed image. A strong correlation and lower RMSE compared to both mask designs. These findings may assist readers in properly evaluating image performance characteristics utilizing the mask/anti-mask subtraction method. Various image evaluation variables for the reconstructed image across both schemes, using different planar square sources and decoding functions, were assessed. Image performance was evaluated using both the mask, the anti-mask, and their difference, before and after decoding. The proposed subtraction method reduced background noise while improving the performance of the rebuilt image. Consequently, subtracted projection images, once decoded, demonstrated enhanced contrast and resolution at full width-at-half-maximum, while SNR remained the same across cases.

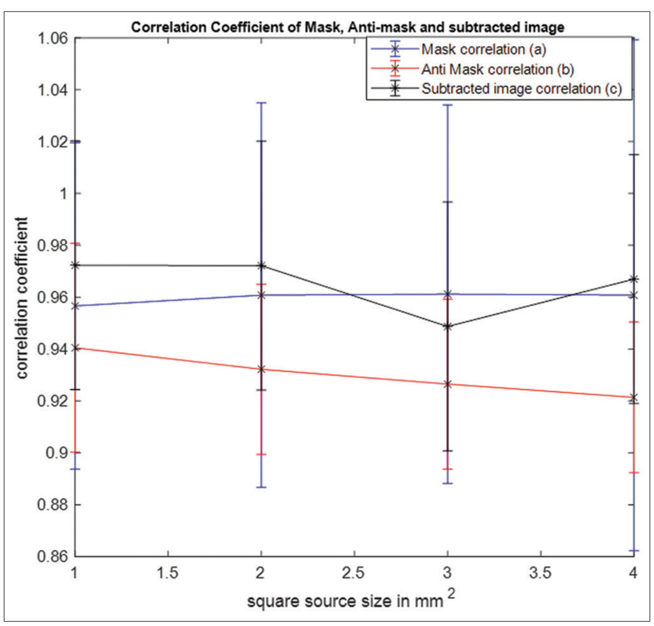

Figure 10: Quantification of the Monte Carlo Simulation data of Modified Uniformly Redundant Array-Coded Aperture camera from (a) the mask, (b) the anti-mask, and (c) the subtracted image. All values obtained from data images of square sources ranging from 1 mm^2 to 4 mm^2

CONCLUSION

In all experiments, results for smaller sources consistently outperformed others, supporting the application of MURA-based coded apertures in small imaging to enhance early-stage lesion detection. In conclusion, the main findings of this work prove that the MURA mask and the MURA anti-mask subtraction approach have positive outcomes that are promising in radionuclide imaging, especially for early breast cancer detection. Future work could focus on the potential application of gold nanoparticles for early breast tumor detection. By utilizing the subtraction method with the proposed imaging technique, it may be possible to identify small lesions with minimal dose requirements. We intend to explore this approach in our future research.

AUTHORS' CONTRIBUTIONS

Conceptualization, K.H., and M.A.A.; Design, K.H., and M.A.A.; Methodology, K.H., M.A.A., H.M.A. and A.S.A.;

Formal Analysis, K.H., M.A.A., and S.H.; Validation, K.H., and M.A.A.; Investigation, K.H., M.A.A., and S.H.; Writing-original manuscript, K.H.; Writing-review and editing, M.A.A., S. H., H.F.A., H.M.A., and A.S.A.; Critically revised manuscript, M.A.A. All authors have read and agreed to the published version of the manuscript.

INSTITUTIONAL REVIEW BOARD STATEMENT

Not applicable.

INFORMED CONSENT STATEMENT

Not applicable.

DATA AVAILABILITY STATEMENT

Data available upon request.

ACKNOWLEDGMENTS

The authors would like to acknowledge the National Plan, Technology and Innovation (MAARIFAH), King Abdulaziz City for Science and Technology, Kingdom of Saudi Arabia, for supporting this work for science. Award Number (12-MED2516-02).

REFERENCES

1. Muraro S, Battistoni G, Kraan A. Challenges in monte carlo simulations as clinical and research tool in particle therapy: A review. Front Phys 2020;8:567800.
2. Kroese DP, Brereton T, Taimre T, Botev ZI. Why the monte carlo method is so important today. Wiley Interdiscip Rev Comput Statis 2014;6:386-92.
3. Park H, Paganetti H, Schuemann J, Jia X, Min CH. Monte carlo methods for device simulations in radiation therapy. Phys Med Biol 2021;66:18TR01.
4. Jan S, Santin G, Strul D, Staelens S, Assié K, Autret D, *et al*. GATE: A simulation toolkit for PET and SPECT. Phys Med Biol 2004;49:4543-61.
5. Cieślak MJ, Gamage KA, Glover R. Coded-aperture imaging systems: Past, present and future development-a review. Radiat Measure 2016;92:59-71.
6. Hussain K, Alnafea MA, Saripan MI, Mahboub D, Mahmud R, Wan Adnan WA, *et al*. An innovative concept of a 3D-coded aperture imaging system proposed for early breast cancer detection. Diagnostics (Basel) 2022;12:2529.
7. Martineau A, Rocchisani JM, Moretti JL. Coded aperture optimization using monte carlo simulations. In: Nuclear Instruments and Methods in Physics Research Section A: Accelerators, Spectrometers, Detectors and Associated Equipment. Vol. 616. Berlin: Springer; 2010. p. 75-80.
8. Levin A, Fergus R, Durand F, Freeman WT. Image and depth from a conventional camera with a coded aperture. ACM Trans Graph (TOG) 2007;26:70-es.
9. Alnafea M. A review of coded aperture families having perfect mathematical imaging properties used for near field imaging application. Asian J Health Res 2018;3:1-18.
10. Solberg TD, DeMarco JJ, Chetty IJ, Mesa AV, Cagnon CH, Li AN, *et al*. A review of radiation dosimetry applications using the MCNP Monte Carlo code. Radiochimica Acta. 2001;89(4-5):337-55.
11. Baró J, Sempau J, Fernández-Varea J, Salvat F. PENELOPE: An algorithm for monte carlo simulation of the penetration and energy loss of electrons and positrons in matter. In: Nuclear Instruments and Methods in Physics Research Section B: Beam Interactions with Materials and Atoms. Vol. 100. Netherlands: Elsevier; 1995. p. 31-46.
12. Agostinelli S, Allison J, Amako K, Apostolakis J, Araújo HM, Arce P, *et al*. GEANT4-a simulation toolkit. In: Nuclear Instruments and Methods in Physics Research Section A: Accelerators, Spectrometers, Detectors and Associated Equipment. Vol. 506. Netherlands: Elsevier; 2003. p. 250-303.
13. Gottesman SR, Fenimore EE. New family of binary arrays for coded aperture imaging. Appl Opt 1989;28:4344-52.
14. Alnafea M, Wells K, Guy M, Spyrou N. Near Field Corrections for Coded Aperture Imaging in Scintimammography. In: Paper Presented at: 2006 IEEE Nuclear Science Symposium Conference Record; 2006.
15. Salvadori J, Labour J, Odille F, Marie PY, Badel JN, Imbert L, *et al*. Monte carlo simulation of digital photon counting PET. EJNMMI Phys 2020;7:23.
16. Staelens S, Buvat I. Monte carlo simulations in nuclear medicine imaging. In: Advances in Biomedical Engineering. Netherlands: Elsevier; 2009. p. 177-209.
17. Bhusal N. Third Generation Gamma Camera SPECT System. United States: Louisiana State University and Agricultural and Mechanical College; 2018.
18. Accorsi R, Lanza RC. Near-field artifact reduction in planar coded aperture imaging. Appl Opt 2001;40:4697-705.
19. Jeong M, Hammig MD. Comparison of gamma ray localization using system matrixes obtained by either MCNP simulations or ray-driven calculations for a coded-aperture imaging system. In: Nuclear Instruments and Methods in Physics Research Section A: Accelerators, Spectrometers, Detectors and Associated Equipment. Vol. 954. Netherlands: Elsevier; 2020. p. 161353.
20. Alnafea M, Wells K, Spyrou N, Saripan M, Guy M, Hinton P. Preliminary results from a Monte Carlo study of breast tumour imaging with low-energy high-resolution collimator and a modified uniformly-redundant array-coded aperture. In: Nuclear Instruments and

Methods in Physics Research Section A: Accelerators, Spectrometers, Detectors and Associated Equipment. Vol. 563. Netherlands: Elsevier; 2006. p. 146-9.
21. Kadri O, Alfuraih A. Monte carlo assessment of coded aperture tool for breast imaging: A mura-mask case study. Nuclear Sci Tech 2019;30:164.
22. Fenimore EE, Cannon TM. Coded aperture imaging with uniformly redundant arrays. Appl Opt 1978;17:337-47.
23. Haboub A, MacDowell AA, Marchesini S, Parkinson DY. Coded aperture imaging for fluorescent x-rays. Rev Sci Instrum 2014;85:063704.
24. Accorsi R, Celentano L, Laccetti P, Lanza R, Marotta M, Mettivier F, *et al*. High-resolution small animal imaging with a coded aperture and a hybrid pixel detector. IEEE Trans Nucl Sci 2008;55:481-90.
25. Dong X, Saripan M, Mahmud R, Mashohor S, Wang A. Determination of the optimum filter for 99mTc SPECT breast imaging using a wire mesh collimator. Pak J Nucl Med 2017;7:9-15.
26. Alnafea M, Wells K, Spyrou N, Guy M. Preliminary monte carlo study of coded aperture imaging with a CZT gamma camera system for scintimammography. In: Nuclear Instruments and Methods in Physics Research Section A: Accelerators, Spectrometers, Detectors and Associated Equipment. Vol. 573. Netherlands: Elsevier; 2007. p. 122-5.
27. Jeong M, Kim G. MCNP-polimi simulation for the compressed-sensing based reconstruction in a coded-aperture imaging CAI extended to partially-coded field-of-view. Nucl Eng Technol 2021;53:199-207.
28. Mukaka MM. Statistics corner: A guide to appropriate use of correlation coefficient in medical research. Malawi Med J 2012;24:69-71.

Source of Support: Nil. **Conflicts of Interest:** None declared.